

AAS 17-618



**APPLICABILITY OF THE MULTI-SPHERE
METHOD TO FLEXIBLE ONE-DIMENSIONAL
CONDUCTING STRUCTURES**

Jordan Maxwell and Hanspeter Schaub

**AAS/AIAA Astrodynamics Specialist
Conference**

Stevenson, WA

August 20–24, 2017

AAS Publications Office, P.O. Box 28130, San Diego, CA 92198

APPLICABILITY OF THE MULTI-SPHERE METHOD TO FLEXIBLE ONE-DIMENSIONAL CONDUCTING STRUCTURES

Jordan Maxwell* and Hanspeter Schaub†

Electrostatic forces and torques are being exploited in space mission concepts such as charged formation flying, inflatable membrane structures, and space debris mitigation technologies. Electrostatic disturbances are also being studied to predict light-weight space debris trajectories. The analysis of these concepts requires faster-than-realtime electrostatic force and torque modeling. The recently developed Multi-Sphere Method (MSM) approximates the electrostatic field about finite bodies using optimally configured conducting spheres as a base function yielding far-faster than realtime force evaluations. The original MSM development makes the assumption that the space object both has a conducting outer surface and has a rigid shape. This paper investigates the effect of relaxing the rigid shape assumption on model accuracy by studying the charged deformation on a flexible one-dimensional structure. The MSM model is initially developed for a non-deformed state, and then retained as the model geometry is varied. The results show that the impact of the rigid shape approximation is promisingly low, approximating the position of all parts of a 6 cm wire to well within 1 cm.

INTRODUCTION

Electrostatic actuation is a promising, touchless method of maneuvering on-orbit. Reference 1 investigated electrostatic deployment of reflective membrane structures as far back as 1966. This idea is revisited more recently in References 2 and 3 which show that electrostatic membranes remain inflated under orbital perturbations. These studies rely on experimental trials to research these electrostatically actuated membrane structures, and no numerical models of the charged membrane dynamics are employed.

Another key application of electrostatic actuation is the problem of space debris in geosynchronous orbit (GEO). Here active charging is employed to create an electrostatic tractor force onto a large, tumbling debris object.⁴⁻⁶ While References 7-11 study the charged debris tugging relative motion control assuming a rigid shape, Aslanov more recently is investigating the impact of spacecraft flexing considerations on the charged relative motion control and demonstrates possible chaotic motions with particular system configurations.¹² High Area-to-Mass Ratio (HAMR) space debris objects represent a danger to existing and future craft in the event of a collision. These objects are postulated to be torn-off mylar sheets whose dynamics are very challenging to model due to being HAMR, having unknown surface properties, as well as being flexible with time-varying shapes. HAMR objects exhibit a large dependence on attitude and are more susceptible to electrostatic perturbations than other craft and objects.¹³ Reference 14 considers a flat plate in GEO and shows that

*Graduate Research Assistant, Aerospace Engineering Sciences, University of Colorado.

†Professor and Glenn L. Murphy Endowed Chair, Associate Chair of Graduate Affairs, Department of Aerospace Engineering Sciences, University of Colorado, 431 UCB, Colorado Center for Astrodynamics Research, Boulder, CO 80309-0431. AAS Fellow

electrostatic torques can affect such an object's attitude, allowing more substantial perturbations such as Solar Radiation Pressure (SRP) to have a greater impact on the object's motion.

Commonly used spacecraft materials such as aluminized mylar are flexible and conductive, and may be torn off due to aging or being hit by micro-meteorites or small space debris. The plasma environment in GEO is such that these materials can achieve voltages as great as -30 kV.¹⁵ Depending on solar activity and the orbit of the flexible sheet, it could deform significantly under Lorentz forces. It could therefore shift from a flat plate-like configuration to become crumpled, exposing far less area. This would affect SRP and drag and therefore the object's orbit.

The original Multi-Sphere Method (MSM) development approximates the electrostatic forces and torques about a general space object, or interacting between multiple closely orbiting space objects, in a faster-than-realtime manner.^{16,17} The main benefit of this method is a drastic improvement in the computational speed required to numerically model electrostatic torques and forces compared to finite element or boundary element solutions. The Volume MSM (VMSM) in particular only requires a small set of spheres as base functions and is able to model the forces to within a few percent of accuracy. This enables far faster-than-realtime numerical simulation of the charged astrodynamics. The MSM models developed thus far all assume the space objects have a fixed shape and conducting outer surface.

This paper investigates the accuracy of applying the MSM model of a fixed shape to a flexible body. This is explored in this first study on this topic by modeling the charged deformation of a flexible one-dimensional structure. Reference 12 also uses a fixed-shape MSM model that is applied to a deformable shape, but the accuracy of this assumption is not studied. In this paper an MSM model is developed for a non-deformed state, and then used for a range of deformation. To maintain a high computational speed, this assumption avoids a more complex scenario where the MSM is reconfigured for each shape deformation. Of interest is how well such a model is able to predict and approximate the actual electrostatic forces and torques acting on this time varying shape. The accuracy is studied for analytical prototypical shape deformations by comparing numerical flexible MSM simulations to experimental charged actuation results.

MULTI-SPHERE METHOD

Overview

MSM is a computationally efficient method of approximating the electrostatic interactions between conductors. Complex spacecraft geometry is replaced with a discrete set of spherical conducting shells to approximate the E -field about a general shape. Two main categories of MSM exist: Volume MSM (VMSM) and Surface MSM (SMSM).¹⁷ VMSM requires that both sphere radii and placement are optimized to match forces and torques,¹⁶ capacitance,¹⁸ or electric fields.¹⁹ SMSM, on the other hand, places spheres equidistantly on the surface of the modeled object, and optimizes only the sphere radii to match any of the physical quantities listed above. For the investigation to follow, a SMSM model using capacitance matching is employed. This paper studies how well the fixed-shape SMSM method can be applied to a flexible one-dimensional string structure.

Figure 1 depicts the SMSM concept applied to an object with a fixed geometry and equi-potential (i.e. conducting) outer surface. The voltage on each of the spheres shown is related to the charge on

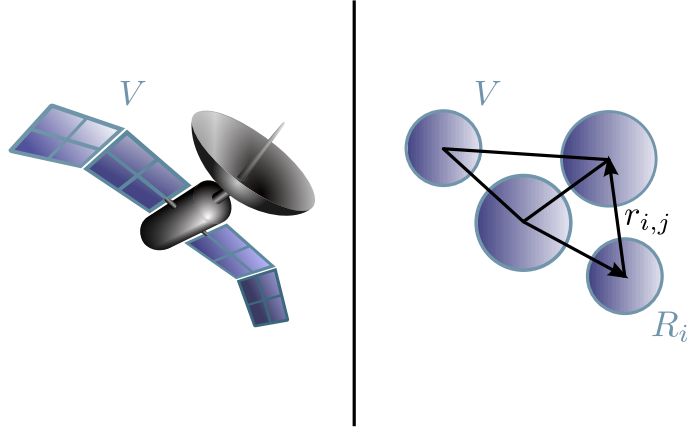


Figure 1: Replacement of complex geometries with SMSM spherical shells

that sphere by

$$V_i = k_c \frac{Q_i}{R_i} + k_c \sum_{j=1, j \neq i}^n \frac{Q_j}{r_{i,j}} \quad (1)$$

where $k_c = 8.99 \times 10^9 \text{ Nm}^2/\text{C}^2$ is Coulomb's constant, R_i is the radius of the i^{th} sphere, and $r_{i,j}$ is the distance between the i^{th} and j^{th} spheres. These relations can be rewritten into a single matrix equation.

$$\begin{pmatrix} V_1 \\ V_2 \\ \vdots \\ V_n \end{pmatrix} = \frac{1}{k_c} \begin{bmatrix} 1/R_1 & 1/r_{1,2} & \dots & 1/r_{1,n} \\ 1/r_{2,1} & 1/R_2 & \dots & 1/r_{2,n} \\ \vdots & \vdots & \ddots & \vdots \\ 1/r_{n,1} & 1/r_{n,2} & \dots & 1/R_n \end{bmatrix} \begin{pmatrix} Q_1 \\ Q_2 \\ \vdots \\ Q_n \end{pmatrix} \rightarrow \mathbf{V} = [S]\mathbf{Q} \quad (2)$$

Here, $[S]$ is called the elastance matrix.²⁰ Another, well-known expression relating charge to voltage, $\mathbf{Q} = [C]\mathbf{V}$ indicates that the capacitance is the inverse of the elastance matrix.

$$\mathbf{Q} = [S]^{-1}\mathbf{V} \quad (3)$$

This form is preferable, as the voltage is usually known and the dynamics are dependent on charge. From Eq. (3), the Coulomb force experienced by the i^{th} sphere in an electric field is

$$F_{C_i} = Q_i \mathbf{E} \quad (4)$$

For rigid structures, the capacitance matrix is constant. For a flexing structure, the relative distances $r_{i,j}$ change as the object flexes as do the charges Q_i . In this paper the application of SMSM to a one-dimensional, flexible conducting structure is explored using a constant capacitance matrix.

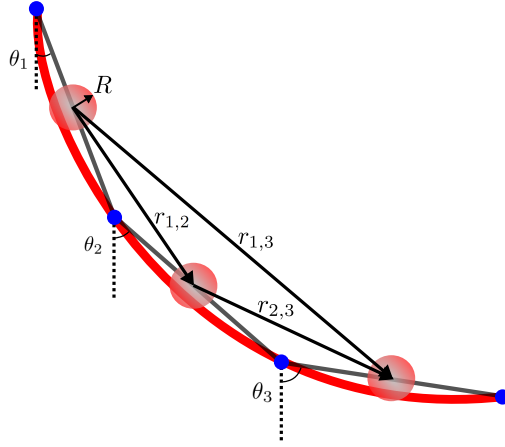


Figure 2: SMSM model of multi-link pendulum

SMSM of a One-Dimensional Wire

Figure 2 shows how a flexible wire is modeled as a multi-link pendulum with SMSM spheres placed evenly at the center of each link. The capacitance of a long, thin, straight wire is given by²¹

$$C = \frac{l}{k_c \Lambda} \left[1 + \frac{1}{\Lambda} (1 - \ln(2)) + \frac{1}{\Lambda^2} \left(1 + (1 - \ln(2))^2 - \frac{\pi^2}{12} \right) + \mathcal{O} \left(\frac{1}{\Lambda^3} \right) \right] \quad (5a)$$

$$\Lambda = \ln \left(\frac{l}{a} \right) \quad (5b)$$

where l is the length of the wire and a is its radius. This equation is valid for large Λ , which requires that the wire length is much greater than the radius. This scalar value is used to optimize the SMSM sphere radius R used in the model. The comparison to the capacitance described in (3) is accomplished by summing the members of the matrix capacitance.

$$C_{\text{scalar}} = \sum_{j=1}^n \sum_{i=1}^n C_{i,j} \quad (6)$$

If the wire changes shape, (5) no longer holds. In reality, all elements of the capacitance matrix should change, but the SMSM model postulated in later sections holds the matrix constant. Figure 3 illustrates the difference between the dynamics resulting from a numerical simulation applying time-varying capacitance versus one with a constant capacitance. The figure shows the percent difference in the inertial angles identified in Figure 2 of a 5-link system between the two cases.

The analysis to follow considers the steady-state response of the system. This allows a final steady-state shape to be predicted subject to charging and external force field interactions. Matching the time-varying response is the topic of future research. Figure 3 shows that, while the dynamics are different between a time-varying and constant capacitance system, the steady-state is nearly identical. Therefore, the use of a constant capacitance matrix optimized using Eq. (5) will not significantly affect the results found in this paper. As further validation, Figure 4 shows the percent difference in the scalar capacitance calculated from Eq. (6). This figure shows that the true, time-varying capacitance does not deviate significantly from the wire capacitance calculated from Eq. (5)

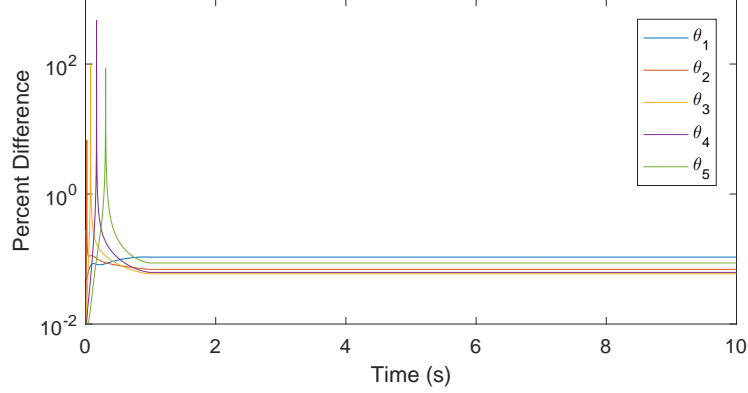


Figure 3: Percent difference between pendulum angles resulting from time-varying capacitance versus constant capacitance

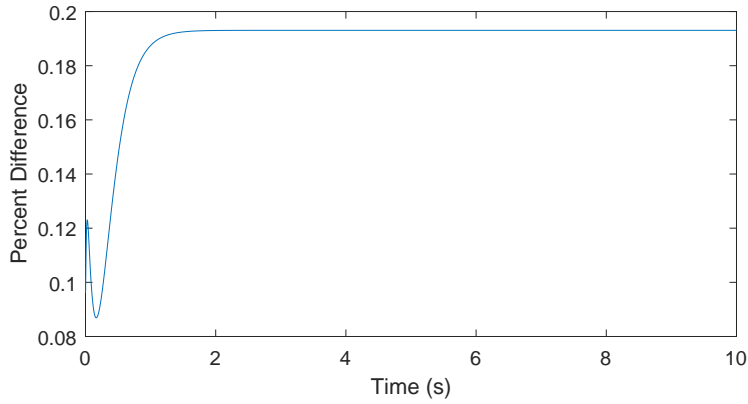


Figure 4: Percent difference between time-varying capacitance and constant capacitance

to which the constant capacitance is optimized. Therefore, Eq. (3) should give a nearly constant value for the charge vector \mathbf{Q} .

A related question relevant to understanding the applicability of SMSM to flexible structures is the accuracy if the capacitance matrix is modified to account for flexing. In this case, the diagonal elements — the radii of the SMSM spheres — are held constant while the off-diagonal elements change to account for deformation. The case of an anchor ring is considered, as it is another configuration for which there is an analytic capacitance. Reference 22 shows that the capacitance of an anchor ring whose cross sectional radius r is small compared to the ring radius ρ is

$$C = \frac{\pi\rho}{k_c \ln(8\rho/r)} \quad (7)$$

Two configurations of a 20-link system similar to that shown in Figure 2 are compared. First, the link is arrayed as a straight line and the SMSM sphere radii are optimized to match the capacitance in Eq. (5). The SMSM system is then rearranged into a ring shape without changing the SMSM sphere locations within each link, or the sphere radii to match the capacitance of the ring. The off-

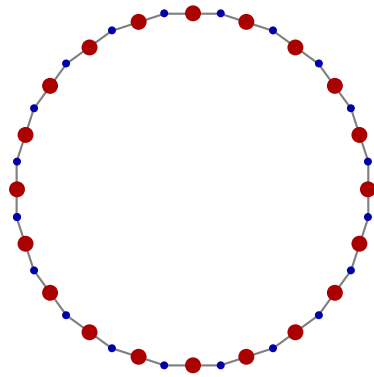


Figure 5: 20-link SMSM model of an anchor ring. The blue circles indicate the hinge locations, while the red accurately represent the SMSM sphere radii optimized using Eq. (5)

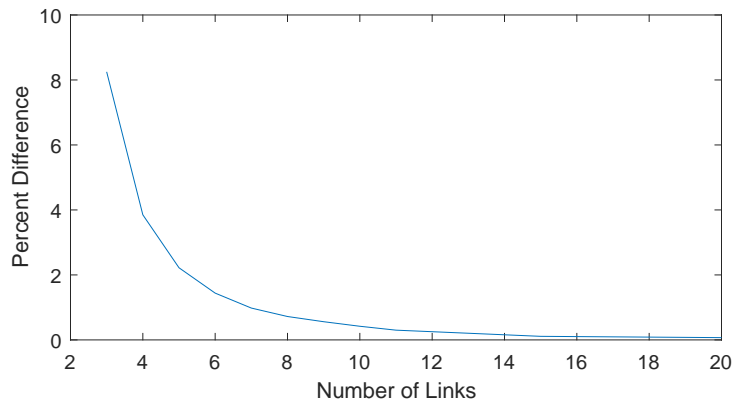


Figure 6: Percent difference between SMSM and analytic anchor ring capacitance for various numbers of links

diagonal terms of the capacitance matrix account for this new geometry and the sum of all matrix elements is compared to the analytical result in Eq. (7).

The resulting non-optimized SMSM capacitance of the ring calculated using the elastance matrix is within 0.1% of the analytic solution given by Eq. (7). A portion of this error is due to the discrete nature of the ring in Figure 5. Figure 6 shows that the difference between the SMSM capacitance and that from Eq. (7) decreases with the number of links. The sign of the error indicates that, up to a 20-link system, the SMSM-calculated capacitance is less than the analytic solution. Given this small error, future work in which a time-varying capacitance is used will likely simulate system dynamics accurately.

CHARGED WIRE EQUATIONS OF MOTION

As shown in Figures 2 and 7, the flexible, conducting wire studied is approximated as a multi-link pendulum system with SMSM spheres placed at the center of each link. The sphere position is one of several tunable parameters, but is held at link-center for simplicity. To account for the stiffness of the wire, torsional springs are simulated at the hinge points of the model. The spring constants

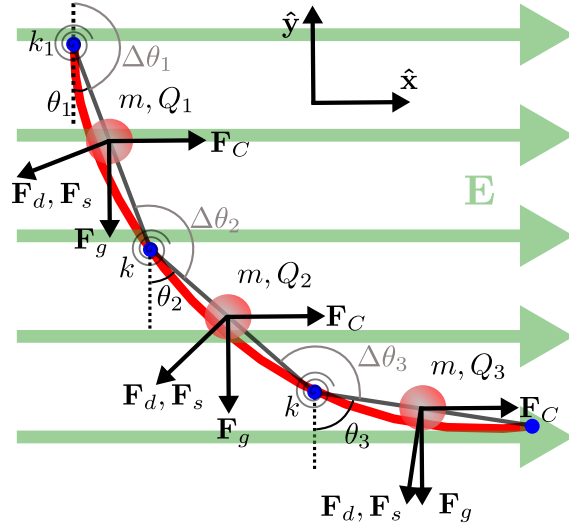


Figure 7: SSM model of a wire showing forces

are main tunable parameter. Note that in Figure 7, the first spring is labeled with a different spring constant, k_1 , than the others. This accounts for an attachment mechanism in the model that affects only the first link. A schematic of the model and forces are shown in Figure 7. Note that the directions of the Coulomb and gravitational forces \mathbf{F}_C , \mathbf{F}_g do not change, while the drag and spring forces, \mathbf{F}_d , \mathbf{F}_s are always opposite of the direction of motion. This model assumes that the wire does not feel its own electric field, so the charges on the SSM model do not repel each other.

The relationship between a conservative force and the corresponding potential energy is

$$U = - \int \Theta \cdot ds \quad (8)$$

where Θ is a force or torque, and ds is the relevant differential. The gravitational force and spring torque are related to the mass of a link m and the relative angles between two links $\Delta\theta$, respectively.

$$\mathbf{F}_g = mg(-\hat{y}) \quad (9a)$$

$$\tau_s = k(\Delta\theta - \Delta\theta_0)(-\Delta\hat{\theta}) \quad (9b)$$

Here g is the gravitational acceleration on Earth's surface, k is the spring constant of the torsional spring, and $\Delta\theta_0$ is the equilibrium angle between the two links. Assuming a perfectly vertical and constant gravitational field

$$U_g = mg(y - y_0) \quad (10)$$

Here, $(y - y_0)$ is the height of the center of mass above the equilibrium position. The spring potential energy is clearly dependent only the relative angles between two links.

$$\begin{aligned} U_s &= - \int_{\Delta\theta_0}^{\Delta\theta} \tau_s \cdot d\Delta\theta' = -k \int_{\Delta\theta_0}^{\Delta\theta} (\Delta\theta' - \Delta\theta_0)(-\Delta\hat{\theta} \cdot \Delta\hat{\theta}) d\Delta\theta' \\ &= \frac{1}{2}k [(\Delta\theta - \Delta\theta_0)^2 - (\Delta\theta_0 - \Delta\theta_0)^2] = \frac{1}{2}k(\Delta\theta - \Delta\theta_0)^2 \quad (11) \end{aligned}$$

As mentioned above, a different spring constant k is used for the first link as for the rest due to the experimental setup. The kinetic energy of each link consists of two components: translation of the center of mass and rotation of a thin rod about its end.

$$T = \frac{1}{2}m\mathbf{v}_{\text{com}} \cdot \mathbf{v}_{\text{com}} + \frac{1}{2}\boldsymbol{\omega}^T I \boldsymbol{\omega} = \frac{1}{2}mv_{\text{com}}^2 + \frac{1}{6}ml^2\dot{\theta}^2 \quad (12)$$

Above, v_{com} is a link's center of mass velocity, l is the length of a link, and $\dot{\theta}$ is the inertial angular velocity of a link. The Lagrangian of the multi-link pendulum system is therefore

$$\mathcal{L} = T - U = \sum_{i=1}^n \left(\frac{1}{2}mv_{\text{com}_i}^2 + \frac{1}{6}ml\dot{\theta}_i^2 - mg(y_i - y_{0_i}) - \frac{1}{2}k_i[\Delta\theta_i - \Delta\theta_{0_i}]^2 \right) \quad (13)$$

where n is the number of links. These n , coupled differential equations are numerically solved simultaneously. The dynamics of the system are determined from Lagrange's Equation.

$$\frac{d}{dt} \left(\frac{\partial \mathcal{L}}{\partial \dot{q}_i} \right) - \frac{\partial \mathcal{L}}{\partial q_i} = Q_i \quad (14)$$

Here, q is a generalized coordinate — in this case the inertial angle of a link — and Q is the sum of generalized, non-conservative forces on a given link. Only two such forces are included in this model: air drag and the Coulomb force. A quadratic drag equation is used. The drag coefficient b is the third tunable parameter in the system and is the same for all links. This value determines the settling time of the system, but does not affect the steady-state position of the multi-link system. It is therefore set to a value that brings the modeled wire to its steady-state quickly to match experiment dynamics.

The Coulomb force is applied as a generalized force because, generally, the charge on each sphere is allowed to vary. Under this condition, the force is not conservative. Since the capacitance matrix is held constant for this model, the charges will not change. In this case, the mathematics works out to be identical to if the Coulomb potential were added as a term in the Lagrangian. This allows for ease of implementation when a time-varying capacitance is used in future model iterations. The forces used to calculate the generalized forces are

$$\mathbf{F}_{D_i} = b\mathbf{v}_{\text{com}_i} \cdot \mathbf{v}_{\text{com}_i} (-\hat{\mathbf{v}}_{\text{com}_i}) \quad (15a)$$

$$\mathbf{F}_{C_i} = Q_i \mathbf{E} \quad (15b)$$

In Eq. (15b), Q_i is the charge on the i^{th} sphere and \mathbf{E} is the external electric field. For this paper, only a flat, constant electric field is considered. Therefore, the Coulomb force experience by each link is constant in time.

The equation for the generalized force on the i^{th} sphere corresponding to a non-conservative force \mathbf{F}_j is

$$Q_i = \sum_{j=1}^N \mathbf{F}_j \cdot \frac{\partial \mathbf{r}_j}{\partial q_i} \quad (16)$$

where j is a sum over N non-conservative forces, i indicates the relevant link, and \mathbf{r}_j is the position at which a given force is applied. Both drag and Coulomb forces are applied at the center of each link as shown in Figure 7.



Figure 8: Experimental setup for comparison to computational steady state modeling

Mathematica is used to generate and solve the full equations of motion of the multi-link model. Numerical solutions to the equations of motion are used because for large numbers of links the analytical forms are extremely complex. The `NDSolve` function is given initial conditions and integrates the equations of motion to provide the inertial angles and their corresponding angular velocities at each timestep.

EXPERIMENT SETUP

Validation of the SMSM system to flexible structures is achieved through comparison with experimental results. The goal of this experiment was to apply a potential to a thin strip, take an image of the steady-state configuration and compare to the results from the model described above.

A parallel plate capacitor is chosen to produce a flat electric field. Expansion to more complicated, possibly time varying electric fields will be the subject of future work.

Figure 8 shows the experiment setup. The stand-in for a one-dimensional conducting structure is a thin strip of aluminumized mylar, which consists of two coatings of 100 \AA thick aluminum on either side of $2 \text{ }\mu\text{m}$ mylar substrate. The aluminum coatings, which are normally isolated by the mylar, are in fact electrically connected due to the cutting process. This strip is attached to the positive plate of the capacitor pictured in Figure 8. This ensures that the strip and positive plate are always at the same potential. Future experiments will explore interactions between thin strips at different potentials from the capacitor's cathode.

A Spellman CZE3000 high voltage power supply (HVPS) controlled by LabVIEW via a National Instruments USB data acquisition (DAQ) unit is used to generate large electric fields within the capacitor and put an excess of charge on the thin strip. An image is then taken of the steady-state response of the strip at voltages ranging from 2400 V to 6150 V. A strip of dimension $6 \text{ cm} \times 2 \text{ mm} \times 2 \text{ }\mu\text{m}$ was used for all experiments.

The commercial finite element solver Maxwell 3D is used to determine the electric field of the

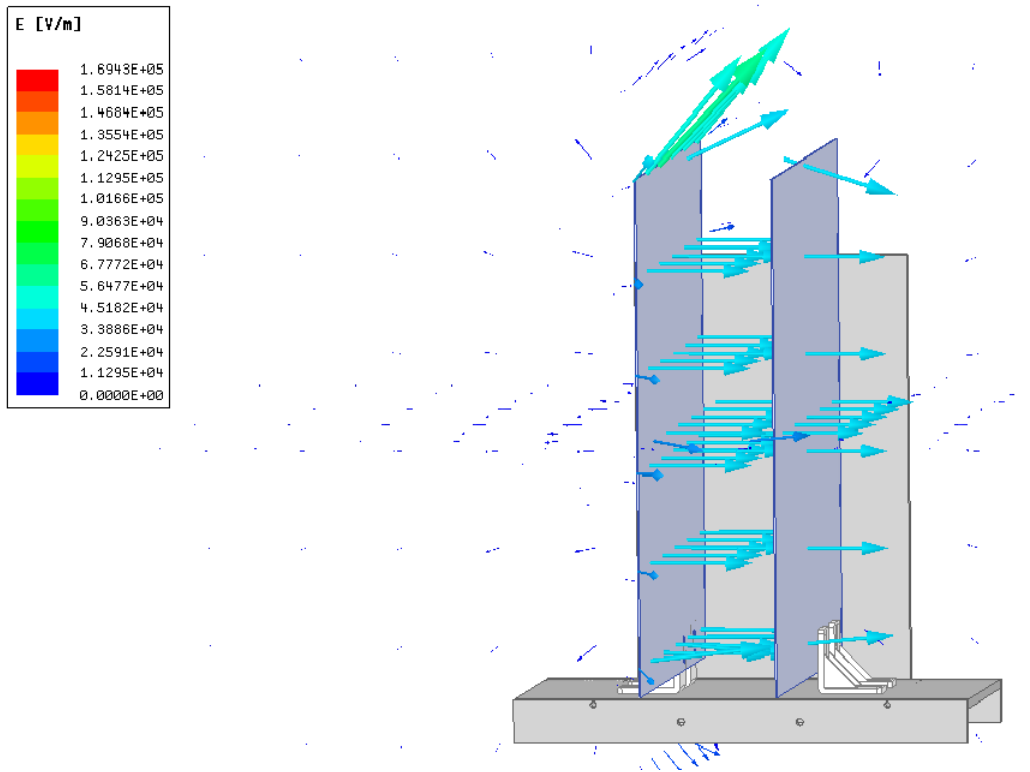


Figure 9: ANSYS Maxwell 3D electric field analysis for experiment structure

parallel plate capacitor used. Figure 9 shows the electric field of a modified experimental system from that shown in Figure 8 imported into Maxwell 3D with accurate material properties and a voltage drop of $\Delta V = 5$ kV across the plates. This simulation was run at several voltages to determine the electric field for a variety of test voltages. All matched the well-known parallel plate capacitor equation: $E = \frac{\Delta V}{d}$ where d is the plate separation. Note that Figure 9 shows that the electric field between the plates is flat everywhere except near edges. The aluminized mylar strip was therefore positioned far from any edges in all experiments.

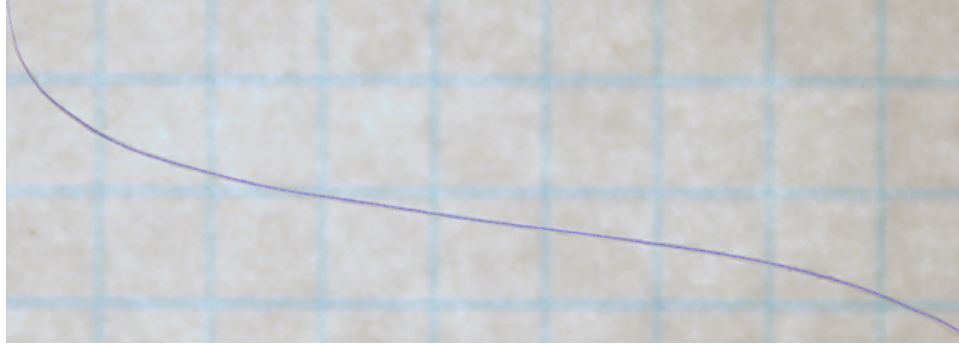
EXPERIMENT ANALYSIS

As various voltages were applied to the cathode of the parallel plate capacitor pictured in Figures 8 and 9, images were taken and loaded into MATLAB for analysis. Edge finding algorithms are used to locate the strip and differentiate it from its surroundings. A piece of grid paper is placed behind the experiment to allow for a conversion from pixels to centimeters. The grid also provides an arbitrary vertical direction two which the image can be aligned. This avoids the need of leveling the camera relative to the experiment.

Once the strip is isolated in the image, the points are fit with a 15-degree polynomial using MATLAB's built-in `polyfit` function. This degree was chosen because the resulting polynomial both matches the curvature of the strip and is well conditioned. The `polyfit` function performed well in fitting all experiment images. The result of edge finding and the final fit of one experiment is shown in Figure 10. Once obtained, the polynomial is used to develop a discrete, n -link system for comparison with the n -link model. The positions of the hinges found from image analysis is



(a) Edge finding result



(b) Fit to image data

Figure 10: Image analysis steps

compared to the steady state hinge positions of the model to determine accuracy.

MODEL INITIALIZATION

One challenge of implementing the numerical model was determining the capacitance of the strip. Recall that Eq. (5) is used to optimize the sphere radii in the SMSM model. This equation is for a thin, cylindrical wire, not a flat strip. However, the analysis method required an extremely flexible object that could also be resolved with a camera for comparison with numerical models. No such wire could be found that was also resolvable with the available camera, but efforts are continuing for the sake of future investigations.

The capacitance of a flat strip does not have a simple, analytic form, and is difficult to determine with programs like Maxwell 3D because of its extremely thin nature. It was decided to use the total volume of aluminum on the aluminized mylar strip to determine the radius of the fictitious wire being used for capacitance matching. The radius a is therefore

$$V_{\text{wire}} = V_{\text{Al}} \rightarrow \pi a^2 L = L w d_{\text{Al}} \rightarrow a = \sqrt{\frac{V_{\text{Al}}}{\pi L}} = \sqrt{\frac{L w d_{\text{Al}}}{\pi L}} = \sqrt{\frac{w d_{\text{Al}}}{\pi}} \quad (17)$$

where w is the width of the strip, L is its length, and d_{Al} is the thickness of the aluminum coating.

The strip initially exhibited some degree of residual stress from the manufacturing, packaging, or cutting processes as shown in Figure 11. Rather than attempt to affect the strip to be more flat, a

similar process to that shown in Figure 10 was used to identify the angles between the n discretized segments. These were then incorporated into the model as the initial inertial angles and as the equilibrium positions for the torsional springs pictured in Figure 7.

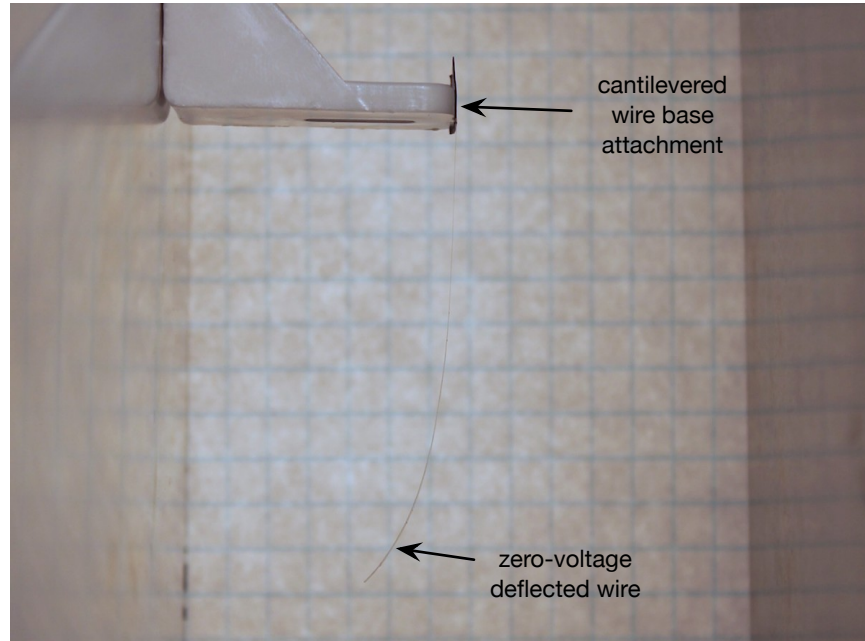


Figure 11: Residual strain on flexible aluminized mylar strip

The method of attaching the strip to the cathode of the parallel plate capacitor with electrical tape creates a hinge about which the strip must bend. This situation is different than bending at any other point in the strip. For this reason, a larger spring constant is used on the first pendulum in the model, as indicated above.

RESULTS

The tuning parameters in the model were the drag coefficient, the aluminized mylar strip capacitance, and the spring constant of the simulated torsional springs. Of these, only the last was changed to match experiment. The system voltages used in experiments are listed in Table 1. These voltages were those applied to the strip and to the cathode of the parallel plate capacitor.

Table 1: System voltages for experiments

Test #	System Voltages (V)
1	6150
2	5400
3	4650
4	3900
5	3150
6	2400

Test 1 is used to select the spring constants in the model, and these spring constants are then maintained for the remainder of the tests. The comparison between the image analysis and the steady state of the numerical model are shown visually in Figure 12. Here, the blue line is the image data representing the unforced strip shown in Figure 11. The yellow line represents the experiment fit for each test similar to that shown in Figure 10b.

It is clear from the figure that as the voltage gets farther from that in Test 1, the model match begins to degrade. Note however that the shape of the wire seems still to match that of the experiment. The SMSM model is developed to match Test 1, so having a good fit there is expected. Further, these experiments were conducted a sequence of voltages, starting with the 6150V of Test 1. As these tests are performed in atmospheric conditions, the air will ionize about this thin charged structure and cause the electrostatic forces to be different. The impact of this is documented in the charged actuation studies in References 23–25. To see such good agreement in this sequential experiment is very promising. Future work will look at methods to de-ionize the air between experiments, as well as to move the experiment inside a vacuum chamber.

An additional source of error could come from the use of linear, torsional springs in the model. Future iterations of this model will explore the use of non-linear spring constants or different mechanisms entirely of accounting for the strip's resistance to bending. Certainly, an additional source of error is the use of a constant capacitance and the assumption that the strip does not feel its own electric field. Additional computational methods will be explored to incorporate these related affects, which were discarded for computational efficiency. Finally, some small portion of error results from current image analysis methods and experimental setup. The application of a wire capacitance to an aluminized mylar strip is an unquantified source of error. A search for extremely flexible, conducting wire will be executed. The difficulty is that most highly flexible structures also tend to be extremely thin and therefore difficult to photograph. This adds significant challenge to the experiment analysis.

Figure 13 shows the distance between the hinge positions in the model and the discretized experiment fit for each test. Note that the maximum distance is less than a centimeter for all tests. Given the simplicity of the model used in this analysis, these results are promising for future work.

CONCLUSIONS

The model applied to match the deformation of a flexible, conducting strip of aluminized mylar had several tunable parameters: a drag coefficient chosen to settle the system quickly, a wire radius chosen to match the volume of conductor on the strip, and the spring constants of the simulated torsion springs at each hinge. Setting these three values to produce desirable results for Test 1, all other experiments were matched to within 1 cm. Given that these experiments are run in a sequential manner in atmospheric conditions, this level of fit is promising for the proposed method. Future work will be conducted in a vacuum chamber and will separate the strip from the cathode of the parallel plate capacitor or other electric field generator. This allows for greater variability in experiments and has the potential to mitigate various complications.

REFERENCES

- [1] John H. Cover, Wolfgang Knauer, and Hans A. Maurer. Lightweigh reflecting structures using electrostatic inflation, 1966.
- [2] Laura A. Stiles, Hanspeter Schaub, Kurt Maute, and Daniel F. Moorer. Electrostatic inflation of membrane space structures. In *AAS/AIAA Astrodynamics Specialist Conference*, Toronto, Canada, Aug. 2–5 2010. Paper No. AIAA-2010–8134.

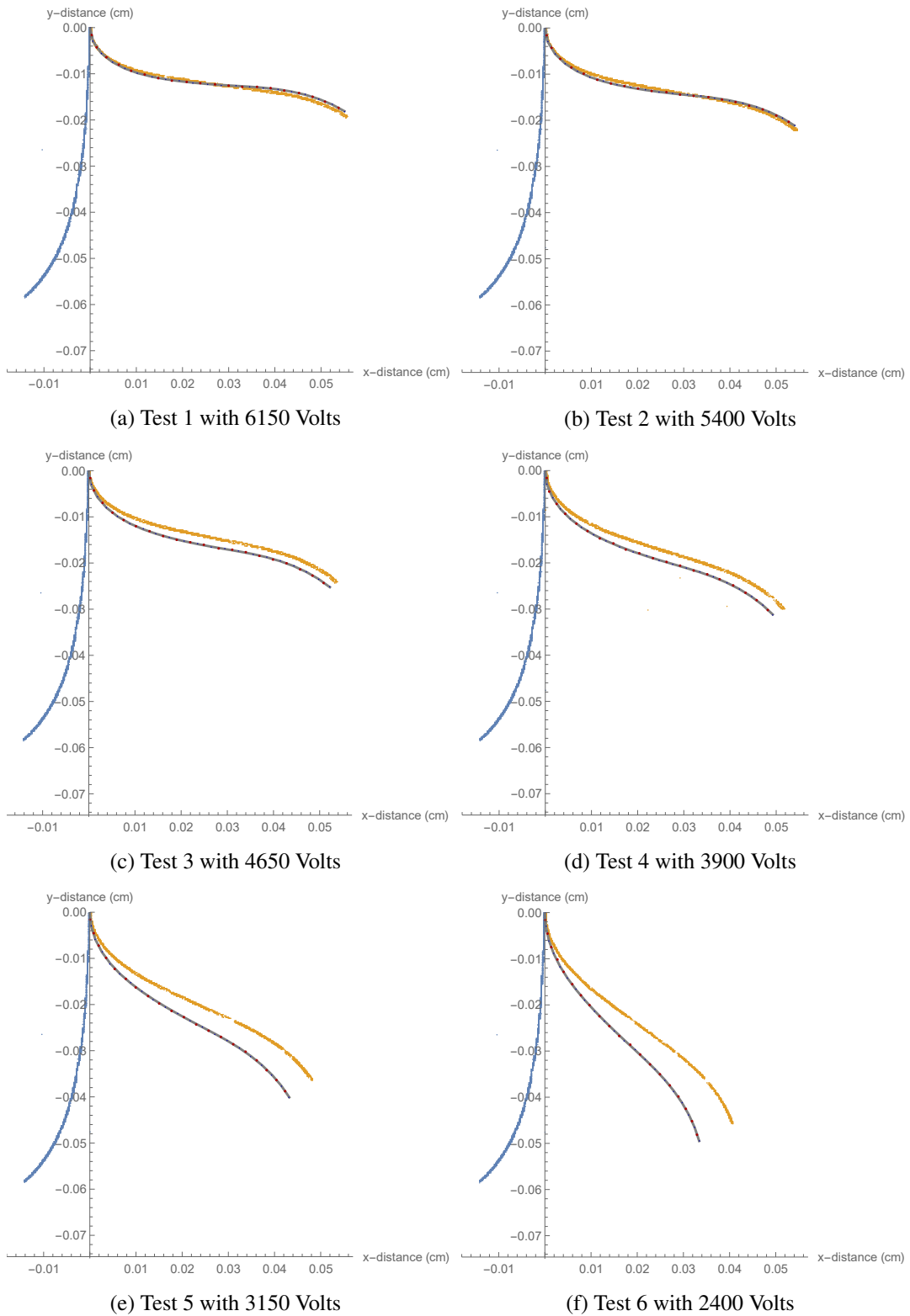


Figure 12: Results of numerical simulations. The blue line represents initial, unforced wire shape while the yellow line represents steady-state experimental configuration. The gray line is the steady-state position calculated using the model described above. On this line, the red spheres represent the placement of the SMSM spheres as well as their actual radii, while the smaller, blue dots represent the breaks between each of the pendulums.

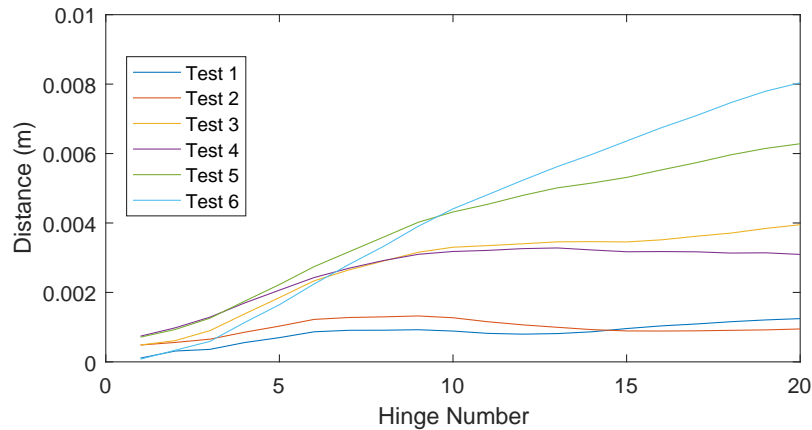


Figure 13: Distance between model and experiment hinge position for each test

- [3] Laura A. Stiles, Hanspeter Schaub, Kurt K. Maute, and Daniel F. Moorer. Electrostatically inflated gossamer space structure voltage requirements due to orbital perturbations. *Acta Astronautica*, 84:109–121, Mar.–Apr. 2013.
- [4] Hanspeter Schaub and Daniel F. Moorer. Geosynchronous large debris reorbiter: Challenges and prospects. *The Journal of the Astronautical Sciences*, 59(1–2):161–176, 2014.
- [5] Daniel F. Moorer and Hanspeter Schaub. Electrostatic spacecraft reorbiter. US Patent 8,205,838 B2, Feb. 17 2011.
- [6] Daniel F. Moorer and Hanspeter Schaub. Hybrid electrostatic space tug. US Patent 0036951-A1, Feb. 17 2011.
- [7] Erik Hogan and Hanspeter Schaub. General high-altitude orbit corrections using electrostatic tugging with charge control. *AIAA Journal of Guidance, Control, and Dynamics*, 38(4):699–705, April 2015.
- [8] Erik A. Hogan and Hanspeter Schaub. Impacts of hot space plasma and ion beam emission on electrostatic tractor performance. *IEEE Transactions on Plasma Science*, 43(9):3115–3129, Sept. 2014.
- [9] Erik A. Hogan and Hanspeter Schaub. Impacts of tug and debris sizes on electrostatic tractor charging performance. *Advances in Space Research*, 55(2):630–638, January 15 2015.
- [10] Erik Hogan and Hanspeter Schaub. Relative motion control for two-spacecraft electrostatic orbit corrections. *AIAA Journal of Guidance, Control, and Dynamics*, 36(1):240–249, Jan. – Feb. 2013.
- [11] Lee E. Z. Jasper and Hanspeter Schaub. Effective sphere modeling for electrostatic forces on a three-dimensional spacecraft shape. In Kyle T. Alfriend, Maruthi Akella, John E. Hurtado, Jer-Nan Juang, and James D. Turner, editors, *Adventures on the Interface of Dynamics and Control*, pages 267–298. Tech Science Press, Duluth, Georgia, 2012.
- [12] Vladimir S. Aslanov. Chaotic dynamics of a satellite with flexible appendages in the coulomb interaction. *Journal of Guidance Control and Dynamics*. (in review).
- [13] Smriti Nandan Paul and Carolin Frueh. Space Debris Charging and its Effect on Orbit Evolution. In *AIAA/AAS Astrodynamics Specialist Conference*, pages 1–31, Long Beach, CA, 2009.
- [14] Joseph Hughes and Hanspeter Schaub. Rapid charged geosynchronous debris perturbation modeling of electromagnetic disturbances. In *AAS Spaceflight Mechanics Meeting*, San Antonio, TX, Feb. 5–9 2017. Paper AAS 17–320.
- [15] Carolin Früh, Dale Ferguson, Chin Lin, and Moriba Jah. The effect of passive electrostatic charging on near-geosynchronous high area-to-mass ratio objects. In *International Astronautical Congress*, volume 64, 2013.
- [16] Daan Stevenson and Hanspeter Schaub. Multi-sphere method for modeling electrostatic forces and torques. *Advances in Space Research*, 51(1):10–20, Jan. 2013.
- [17] Daan Stevenson and Hanspeter Schaub. Optimization of sphere population for electrostatic multi sphere model. *IEEE Transactions on Plasma Science*, 41(12):3526–3535, Dec. 2013.
- [18] Philip Chow, Joseph Hughes, Trevor Bennett, and Hanspeter Schaub. Automated sphere geometry optimization for the volume multi-sphere method. In *AAS/AIAA Spaceflight Mechanics Meeting*, Napa Valley, California, Feb. 14–18 2016. Paper No. AAS-16-472.

- [19] Gabriel Ingram, Joseph Hughes, Trevor Bennett, Christine Hartzell, and Hanspeter Schaub. Autonomous volume multi-sphere-model development using electric field matching. In *AAS Spaceflight Mechanics Meeting*, San Antonio, TX, Feb. 5–9 2017. Paper AAS 17-451.
- [20] W. R. Smythe. *Static and Dynamic Electricity*. McGraw–Hill, 3rd edition, 1968.
- [21] J. D. Jackson. Charge density on thin straight wire , revisited Charge density on thin straight wire , revisited. *American Journal of Physics*, 789(68), 2000.
- [22] T.S.E Thomas. The Capacitance of an Anchor Ring. *Australian Journal of Physics*, 7:347, 1954.
- [23] Carl R. Seubert and Hanspeter Schaub. Closed-loop one-dimensional charged relative motion experiments simululating constrained orbital motion. *AIAA Journal of Guidance, Control, and Dynamics*, 33(6):1856–1865, Nov.–Dec 2009.
- [24] Daan Stevenson and Hanspeter Schaub. Terrestrial testbed for remote coulomb spacecraft rotation control. *International Journal of Space Science and Engineering*, 2(1):96–112, 2014.
- [25] Daan Stevenson and Hanspeter Schaub. Electrostatic spacecraft rate and attitude control - experimental results and performance considerations. *Acta Astronautica*, 119:22–33, Feb. – March 2016.